Signal, Image and Video Processing
https://doi.org/10.1007/s11760-022-02226-y

ORIGINAL PAPER

Fluorescence microscopy image noise reduction using IEMD-based adaptive thresholding approach

Tushar Rasal[1] · Thangaraj Veerakumar[1] · Badri Narayan Subudhi[2] · Sankaralingam Esakkirajan[3]

Received: 12 March 2021 / Revised: 24 December 2021 / Accepted: 25 March 2022

Abstract
Fluorescence microscopy is an important investigation tool for discoveries in the field of biological sciences. In this paper, we propose an adaptive thresholding technique-based improved empirical mode decomposition (IEMD) for denoising of heavily degraded images labeled with Fluorescent proteins. These images are widely used by a computational biologists to analyze the biological functions of different species. A variance stabilization transformation is applied as preprocessing step. The multi-scale Wiener filtering approach is used as the first step for accurate image deconvolution. In the subsequent steps, IEMD is performed to obtain different series of intrinsic mode functions (IMFs) which are further separated into noise and signal-significant IMFs based on Cosine similarity index. The IMF adaptive thresholding technique is used which filter-out the unwanted frequency coefficients related to mixed Poisson–Gaussian noise (MPG). The thresholded output IMFs are combined with signal significant IMFs in the third step. Finally, the mean square deviation (MSD) is minimized using mixed Poisson–Gaussian unbiased risk estimate (MPGURE). To evaluate the effectiveness of the proposed scheme, we have compared the results of the proposed scheme with those of the five state-of-the-art techniques. The simulation results validate, the effectiveness of the proposed method. The proposed algorithm achieves better performance in terms of four quantitative evaluation measures by reducing the effect of noise.

Keywords Empirical mode decomposition · Intrinsic mode function · Mixed Poisson–Gaussian noise · Mixed Poisson–Gaussian unbiased risk estimate

1 Introduction

Fluorescence microscopy is a powerful investigation tool used for biological research nowadays, especially with the development of labeling techniques [1]. The innovation and research of labeling the subtle details with Fluorescence tags allows to take a deep look into the cellular world of biology. The biological objects of interest specifically labeled with genetically engineered proteins (e.g., organic dyes, green fluorescence protein (GFP)) are used for non-invasive imaging of living cells [2]. Fluorescent marker precisely empowers visualization of biological structures, cell–cell interaction, sub-microscopic details of tissues. A better understanding of cellular dynamics of living cells is possible with Fluorescent microscopy, so it is widely used in the field of neurobiology, biomedical, and material sciences [3].

In Fluorescent microscopy, the images are acquired under low light conditions with limited exposure time. So the observed images under a microscope are having low photon count and results in low signal-to-noise ratio (SNR). Making an interpretation from such inseparable and heavily degraded observation is the most challenging problem for many biological researchers [4].

Many image restoration techniques are found to be ever-growing in the field of super-resolution microscopy imaging

✉ Thangaraj Veerakumar
tveerakumar@nitgoa.ac.in

Tushar Rasal
tusharoptimus@gmail.com

Badri Narayan Subudhi
subudhi.badri@iitjammu.ac.in

Sankaralingam Esakkirajan
rajanesakki@yahoo.com

[1] Department of Electronics and Communication Engineering, National Institute of Technology Goa, Ponda 403401, India

[2] Department of Electrical Engineering, Indian Institute of Technology Jammu, Jagti 181121, India

[3] Department of Instrumentation and Control Systems Engineering, PSG College of Technology, Coimbatore 641004, India

Published online: 19 April 2022

for addressing the problem of low SNR. The restoration algorithms are available in the literature use the principle of variance stabilizing transformation (VST) for transforming the Poisson variables to Gaussian variables [5]. Total variation-based methods and Richardson–Lucy (RL) algorithms [4] are very efficient for images which are piece-wise constant. It uses convex optimization schemes but suffers from artifacts like a staircase effects. In [6], the total variation iterated condition expectation (TV-ICE) method uses an iterative local update scheme of pixels to remove the staircase effects. The TV-ICE re-modified with the Bayesian frameworks [7] provides great improvement in terms of computational efficiency but more sensitive to the noise level. The Poisson expectation maximum total variance (Poisson EM-TV) approach [8] uses weighted data-fidelity model and divergence term with convex optimization which works better for Poisson noise. In the Bayesian framework, the total variation maximum a posterior (TV-MAP) approach [9] is introduced which gives better results than TV-ICE approach.

Early work for denoising such as dictionary-based K-SVD [10] provides better denoising performance, but the only disadvantage is that the quality of restored images depends on the training set. This limits the performance of K-SVD for high noise density data. The stochastically connected random fields (SRF) approach eliminates the noise effectively, but it is more suspected to noise under low photon count conditions. The overall aims and interests of biological research deal with challenges such as low light conditions, limited exposure time, non-representative intensity fluctuations, MPG noise, and image deconvolution. These challenges can be handled by devoted noise removing algorithms that relies on composite Gaussian–Poisson noise model and concreted to high noise level.

This article is organized as follows: Sect. 2 explores an overview of the proposed image restoration mechanism with a block diagram. The detailed qualitative and quantitative analysis with detailed discussion is described in Sect. 3. Finally, in Sect. 4 the overall summary is outlined as conclusions.

2 Proposed methodology

The detailed block diagram of the proposed restoration mechanism is shown in Fig. 1. The blurred and noisy image is considered as an input for the proposed technique. The variance stabilization transformation is used as the first step in image denoising mechanism. In the next step of processing, the multi-scale Wiener filtering approach is used to filter-out the effect of blurring caused by microscopic components.

In the next step, improved empirical mode decomposition (IEMD) is performed on the filtered images to get different series of IMFs. The obtained IMFs are having much better

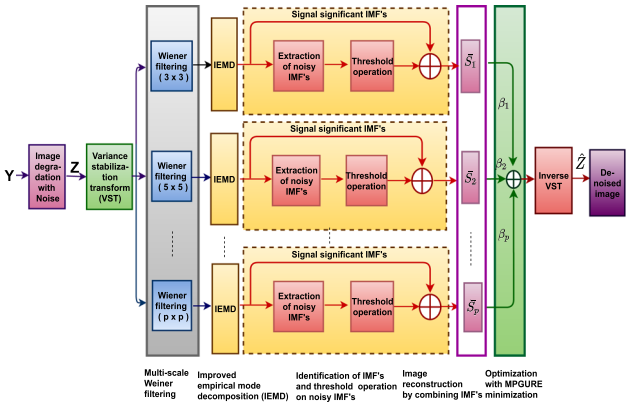

Fig. 1 The block diagram of the proposed image restoration mechanism

frequency resolution. The IMFs identification scheme based on Cosine similarity index followed by adaptive thresholding is shown in the subsequent step of the block diagram.

In the next step, the optimization framework based on minimization of mixed Poisson–Gaussian unbiased risk estimate (MPGURE) is shown. The different optimum coefficients used for reconstruction are evaluated based on the minimization of MPGURE. Finally, the inverse variance stabilization transformation is applied to obtain the final estimated noise-free image.

2.1 Noise model for fluorescence microscopy

We have incorporated a mixed Poisson–Gaussian (MPG) noise model for noise degradation [4,11]. The biological specimen observed under microscopes can be represented as,

$$Z = \alpha \mathcal{P}\left(\frac{Hy}{\alpha}\right) + \mathcal{N}\left(0, \sigma^2\right), \tag{1}$$

where Z is the observed image, y is the noise-free image, H is the point spread function (PSF) of the microscope, $\mathcal{P}(.)$ is the realization of Poisson noise and α is the scaling factor which controls the strength of the Poisson noise. $\mathcal{N}\left(0, \sigma^2\right)$ represents the Gaussian noise with 0 mean and variance σ^2.

2.2 Variance stabilization transformed (VST) and multi-scale wiener filtering approach

The observed image Z has variance which is directly proportional to true image intensity λ. In order to stabilize the variance of Z, we used variance stabilization transformation as, $Y = T(Z)$ which makes $Var(Y)$ asymptotically constant irrespective of λ as,

$$T(Z) = b.sgn(Z + c)\,|Z + c|^{1/2}, \tag{2}$$

where b is the normalizing factor, $sgn(.)$ is the sign function. We have considered the value of c as 0.0625 [12].

The deconvolution with multi-scale Wiener filtering approach filters-out the effect of blurring and to provides better superlative resolution. In general, l number of Wiener filters with different size Gaussian kernels are used for deconvolution process.

2.3 Improved empirical mode decomposition (IEMD)

The EMD uses two-dimensional sifting process which extracts a finite number of oscillatory components called IMF's directly from the image. This can be formulated as;

$$I = \sum_{j=0}^{J} I_{\text{mode}}(j) + I_{\text{res}}, \tag{3}$$

where I is the original image, J indicates the total number of IMFs, $I_{\text{mode}}(j)$ is the jth mode (or IMF) of an observed image and I_{res} is the final residual component.

For extrema detection (minima or maxima), we used neighboring window and eight connectivity within image intensity function. The selection of extreme value is done within eight adjacent points. The radial basis function (RBF) $B(w)$ can be expressed as,

$$B(w) = q_m(w) + \sum_{g=1}^{F} \lambda_g \Phi\left(\|w - w_g\|\right), \tag{4}$$

where $w \in \Re^d$ and $\lambda_g \in \Re$, $q_m(w)$ is the linear or quadratic low degree polynomial which is a member of mth degree polynomials, λ_g is the gth coefficients of RBF, F indicates the total number of RBF, Φ is the real-valued basis function, $\|.\|$ indicates the Euclidean norm and w_g is the center of RBF. The stopping criteria used in the sifting process is given as,

$$(S_d(i) - S_d(i-1)) < (Pr * S_d(i)), \tag{5}$$

where S_d is the standard deviation, $(S_d(i) - S_d(i-1))$ indicates the difference between consecutive standard deviations and Pr is the precision of EMD for extrema detection and considered as 0.00003. The stopping criteria used as, the difference between two relative standard deviations computed from two successive sifting results $I_{\text{res}_j}(i-1)$ and $I_{\text{res}_j}(i)$, which is less than threshold value. The standard deviation can be obtained as,

$$S_d(i) = \sum_{u=0}^{U}\sum_{v=0}^{V}\left[\frac{\left|I_{\text{res}_j}(i-1)(u,v) - I_{\text{res}_j}(i)(u,v)\right|^2}{I^2_{\text{res}_j}(i-1)(u,v)}\right], \tag{6}$$

where $I_{\text{res}_j}(i-1)$ and $I_{\text{res}_j}(i)$ indicate the two successive results of sifting process. The different series of IMFs are obtained with improved empirically mode decomposition.

2.4 Identification of signal-significant and noise-significant IMFs

We assume an index denoted by Q for distinguishing the different IMFs. The input image is decomposed by IEMD as,

$$I = \sum_{j=0}^{Q-1} I_{\text{mode}}(j) + \sum_{j=Q}^{J} I_{\text{mode}}(j) + I_{\text{res}}, \tag{7}$$

where $I_{\text{mode}}(j)$ indicates jth IMF, I_{res} indicates the residual component. Here, the useful IMFs are selected for partial reconstruction called as IEMD-corPR [13]. This can be given as,

$$\hat{I} = \sum_{j=Q}^{J} I_{\text{mode}}(j) + I_{\text{res}}. \tag{8}$$

The index Q can be calculated with Cosine similarity measure between original data and estimated modes. The estimated mode $\hat{I}_m$ can be calculated as,

$$\hat{I}_m = I - \sum_{j=1}^{m} I_{\text{mode}}(j). \tag{9}$$

The Cosine similarity measure denoted by 'Csim' between original data and the estimated modes can be given as,

$$\text{Csim}(\hat{I}_m, I) = \frac{\sum_i \hat{I}_m(i) I(i)}{\sqrt{\sum_i \hat{I}^2_m(i)}\sqrt{\sum_i I^2(i)}} = \frac{\left\langle \hat{I}_m, I \right\rangle}{\left\|\hat{I}_m\right\| \|I\|}, \tag{10}$$

where $\hat{I}(i)$ and $I(i)$ indicates the intensity values of ith pixel in estimated mode and observed image, respectively. Here, N denotes the total number of pixels in image and i varies from 1 to N.

However, the 'Csim' measure between $\hat{I}_m$ and I having a drawback of shift variations. In this work, we considered the centered version of the images which is shift-invariant. The $\text{Csim}(\hat{I} - \hat{I}_{\text{mean}}, I - I_{\text{mean}})$ denoted by $\mathcal{C}(f)$ can be given as,

$$\mathcal{C}(f) = \frac{(\sum_i \hat{I}_m(i) - \hat{I}_{\text{mean}})(I_m(i) - I_{\text{mean}})}{\sqrt{\sum_i (\hat{I}_m(i) - \hat{I}_{\text{mean}})^2}\sqrt{\sum_i (I_m(i) - I_{\text{mean}})^2}}, \tag{11}$$

where $\hat{I}_{\text{mean}}$ and I_{mean} indicates the mean value of the estimated mode and the observed image, respectively. f is the

index when $\mathcal{C}(f)$ starts with having value smaller than some constant which is set empirically as 0.85. The index Q used for IMFs identification can be calculated as,

$$Q = \arg\max\{\mathcal{C}(f) > 0.85\} + 1, \tag{12}$$

where f varies from 0 to J, the maximum value of $\mathcal{C}(f)$ is considered in order to evaluate index Q.

2.5 Intrinsic Mode Function Adaptive Thresholding Scheme

The modes having index less than Q are identified as noise dominant IMFs and threshold operation is performed on it. The modes having index greater than Q are excluded from threshold operation. The calculation of IMF adaptive universal threshold can be given as [13],

$$T_a = \eta\sqrt{2J_r \ln M}, \tag{13}$$

where η is a constant which is empirically set to 0.5, J_r is the energy of IMF, $r = 1, 2, 3, .., J-1$ and M is the total number of elements within image.

$$J_r = \frac{J_1^2}{\lambda}\zeta^{-r}, \tag{14}$$

where $r = 2, 3.., J-1$. The parameters ζ and λ are chosen based upon the number of iteration during sifting process and IMFs. We selected $\lambda = 0.719$ and $\zeta = 2.01$. Here, J_1^2 indicates energy of the first IMF which can be calculated as,

$$J_1 = \frac{median\,|IMF_1|^2}{0.6745}, \tag{15}$$

The thresholding function used to filter-out the noisy component is given as,

$$\Phi_{thr}^{k}(IMF_j(U_d{}^c)) = \begin{cases} 0, & \text{if, } |\,IMF_j(\Upsilon_d{}^c)\,| \le T_a \\ IMF_j(U_d{}^c)\dfrac{|\,IMF_j(\Upsilon_d{}^c)|-T_a}{|\,IMF_j(\Upsilon_d{}^c)|}, & \text{else;} \end{cases} \tag{16}$$

where IMF_j is the jth mode, $U_d{}^c = [U_d{}^c U_{d+1}{}^c]$ indicates the cth zero crossing interval, $\Upsilon_d{}^c$ indicates the extreme points within interval of $[U_d{}^c U_{d+1}{}^c]$ and T_a indicates the threshold.

The threshold operation is only performed on noise-dominant IMFs. The different noise-free IMFs can be further used for reconstruction as,

$$\bar{S}_k = \sum_{j=0}^{Q-1}\Phi_{thr}^{k}(IMF_j) + \sum_{j=Q}^{J} I_{\text{mode}}^{k}(j) + I_{\text{res}}^{k}, \tag{17}$$

where $\Phi_{thr}^{k}(IMF_j)$ indicates the IMF obtained after performing threshold operation, I_{mode}^{k} is the noise-free IMF. $\bar{S}_k$ is the reconstructed image obtained by combining all IMFs, and the suffix k indicates the outputs for kth Wiener filtering stage. The different reconstructed images $\bar{S}_1, \bar{S}_2 \ldots, \bar{S}_p$ can be used for further optimization.

2.6 MPGURE minimization

The noise-free and thresholded output IMFs are simply combined as,

$$\hat{S} = \sum_{k=1}^{p}\beta_k\bar{S}_k = \beta_1\bar{S}_1 + \beta_2\bar{S}_2 + \cdots + \beta_p\bar{S}_p, \tag{18}$$

where $\hat{S}$ is the reconstructed output before inverse VST, k represents the total number of optimized coefficients: $\beta_1, \beta_2 \ldots, \beta_k$. The MSD minimization with MPGURE can be used to find out the optimal coefficients given as,

$$\text{MSD} = \frac{1}{N}E\left[\left\|\bar{S} - S\right\|_2^2\right] = \arg\min_{\beta_k}\left\|\sum_{k=1}^{p}\beta_k\bar{S}_k - S\right\|_2^2 \tag{19}$$

subjected to constraints as sum of the all optimized coefficients equal to 1, i.e., $\sum_{k=1}^{p}\beta_k = 1$, where p indicates the stages in multi-scale Wiener filtering. $\bar{S}$ is the image obtained by recombining IMFs using Eq. (17), S is the noisy image. $E[.]$, $\|.\|_2$ indicates the expectation and L_2-norm operator, respectively. The direct evaluation of MSD is impossible without knowledge of ground truth. The approximation is made with MPGURE as the expectation of MPGURE is same as the expectation of MSD which completely relies on noisy observations [14]. The MSD can be calculated as,

$$\text{MSD} = \frac{1}{N}E\left[\left\|\bar{S} - S\right\|_2^2\right] = \frac{1}{N}E\left[\text{MPGURE}\right]. \tag{20}$$

The theoretical proofs of Eq. (20) can be found easily in [14, 15]. The approximation to MSD has been made by estimating MPGURE as,

$$\text{MPGURE} = \frac{1}{N}\Big(\left\|\bar{S}\right\|_2^2 + \|S\|_2^2 - 2\left\langle S\cdot\bar{S}^{-\alpha}\right\rangle + 2\sigma^2\nabla\bar{S}^{-\alpha}(S) - \alpha S\Big) - \sigma^2, \tag{21}$$

where $\bar{S}^{-\alpha}$ is the function of real-valued image, ' $\langle\cdot\rangle$ ' indicates the inner product between vectored image, α is the gain for the Poisson process, σ is the standard deviation and ∇ is the divergence operator.

The first-order Taylor's series expansion of the estimated image of real-valued function can be calculated as, $\bar{S}^{-\alpha} \approx \bar{S}$-

$\alpha\ \partial\bar{S}$. The modification of Eq. (21) can be written as,

$$\text{MPGURE} = \frac{1}{N}\left(\left\|\bar{S}-S\right\|_2^2 - 2\left\langle \alpha S + \sigma^2 1\cdot\partial\bar{S}\right\rangle - 2\sigma^2\alpha\left\langle 1\cdot\partial^2\bar{S}\right\rangle - \alpha\left\langle 1\cdot S\right\rangle\right) - \sigma^2. \tag{22}$$

The evaluation of some terms in Eq. (22); $\bar{S}^{-\alpha}$, $\partial\bar{S}$ and $\partial^2\bar{S}$ become practically unrealistic. In photon-starved applications, the Poisson noise is the dominant source of noise, so the effect of Gaussian noise can be neglected [4] which can be approximated with $\sigma = 1$ [14,15] results in,

$$\text{MPGURE} = \frac{1}{N}\left(\left\|\theta_n(S)\right\|_2^2 + 2\nabla\theta_n(S) - 2\alpha\cdot\theta_n(S) - 2\alpha\cdot S\right) - 1, \tag{23}$$

where $\theta_n(S)$ is the difference between the noisy and the noise-free image which can be expressed as,

$$\theta_n(S) = \{\theta_n\}_{n=1}^{\delta_s} = \bar{S} - S,\ \nabla\theta = \sum_{n=1}^{\delta_s}\frac{\partial\theta_n}{\partial S}, \tag{24}$$

where θ_n is the error between nth estimated and noisy images, δ_s is the total number of images.

The expectation of MSD in terms of $\theta_n(S)$ can be obtained as,

$$E\left[\left\|\bar{S}-S\right\|_2^2\right] = \delta_s + E\left[\left\|\theta_n(S)\right\|_2^2\right] + 2\nabla\theta_n(S) - \alpha S, \tag{25}$$

where δ_s is constant which depends upon the variance of image, $\|.\|_2^2$ indicates the L_2 norm square for the inside term and E[.] is the expectation operator. Here, $\theta_n(S)$ indicates the difference between noisy and noise-free images. The MPGURE estimate for the image can be approximated using Eq. (16) as,

$$\text{MPGURE} = \delta_s + \sum_1^n\left\|\theta_n(S)\right\|_2^2 + 2\sum_1^n\frac{\partial\theta_n}{\partial S} - \sum_1^n\alpha S. \tag{26}$$

This is the unbiased risk estimate for MSD. We have calculated the optimal coefficients which minimizes the MSD as,

$$\beta_k = arg\min_{\beta_k} E\left[\text{MPGURE}\right]. \tag{27}$$

The final denoised image with inverse VST as, $\hat{Z} = T^{-1}\left(\hat{S}\right)$, where $\hat{S}$ is the reconstructed image and $\hat{Z}$ is the final estimated image.

In the proposed algorithm, the steps involved for denoising are given in Algorithm 1.

Algorithm 1: Denoising scheme based IEMD and IMF's adaptive threshold

Result: Noise-free output images.
Step 1. Choose the input noisy and blurred image;
Step 2. Apply non-linear transformation and multi-scale Wiener filtering;
Step 3. **while** $W = 1$ *to* p **do**
  Apply EMD with eq. (3);
  Identification of noise-dominant and signal-dominant IMFs based index Q evaluated with eq. (12) ;
  for $q = 1$ *to* $s-1$ **do**
    Evaluate threshold using eq. (13);
    Apply threshold on different coefficients as per criteria;
    if $\left|IMF_j(\Upsilon_k{}^c)\right| \le T_a$ **then**
      $\Phi_{thr}(IMF_j(U_k{}^c)) = 0$;
    else
      $IMF_j(U_k{}^c)\frac{\left|IMF_j(\Upsilon_k{}^c)\right|-T_a}{\left|IMF_j(\Upsilon_k{}^c)\right|}$;
    end
  end
  Recombine the thresholded IMF's using eq. (17) and obtain the different outputs $\bar{S_1}, \bar{S_2},\ldots,\bar{S_p}$;
end
Step 4. Obtain different optimal coefficients by minimizing MPGURE using eq. (26) and eq. (27) with linear system of equations $Ax = b$;
Step 5. Obtained final output by combining the different optimal coefficients using eq. (18);
Step 6. Apply the inverse variance stabilization transformation with eq. (19) ;

3 Experiments and results analysis

The proposed algorithm is implemented in Intel i3, 2 GHz PC with 8GB RAM computer. The source code is run on MATLAB R2018a software. We have compared results of the proposed scheme with those of five different competing state-of-the-art algorithms which are specially designed to tackle MPG noise such as PURE-LET [15], SPIRAL-TAP [16], NLPCA [10], TV-MAP [17] and PNLW [18]. The source code of the proposed scheme is available at [1]

3.1 Description of the database and performance metrics

In this work, 14 different types of Fluorescent microscopy image datasets are used for evaluation. Each dataset is obtained by labeling the specimens with various types of Fluorescent proteins. Fluorescence microscopy images are taken from the yeast resource center public image repository (YRCPIR) [19] and cell tracking challenge database [20].

[1] https://github.com/tusharrasal/Fluorescence-Microscopy-Image-Noise-Reduction-using-IEMD-based-Adaptive-Thresholding-Approach.git.

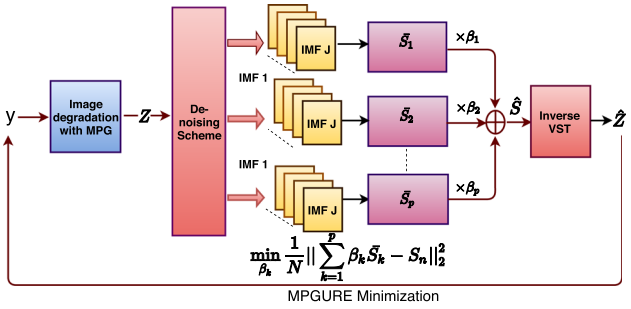

Fig. 2 The optimization approach

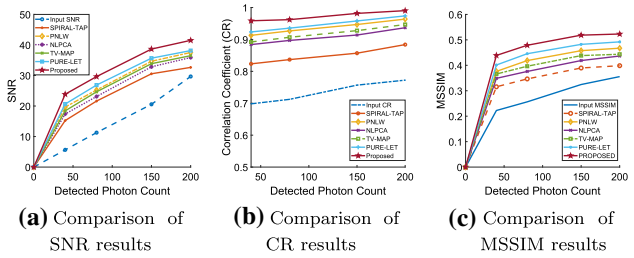

(a) Comparison of SNR results **(b)** Comparison of CR results **(c)** Comparison of MSSIM results

Fig. 3 The simulation results for Fluocells image

3.2 Parameters tuning

For better image denoising results, values of these parameters are fixed according to some preliminary experiments. The proposed method needs a training process. We used a small subset of images (containing 56 different images) to tune the parameters, and average value of parameters is considered. We have divided the considered images into training and testing. For training, we have used 4 images from each fluorescent type. Hence, considering 14 different sets, we have used $14 \times 4 = 56$ images for training our model. Due to selection of different images from different datasets, the performance of proposed algorithm is generalized. It provides optimal performance over the parameter variations. For validation, we used remaining images from each fluorescent type. The presented results do not include the training images. The parameters such as number of Wiener filters (l), total number of optimized coefficients (k), λ, ς are selected based on minimizing an objective function (MSE) and testing the quantitative evaluation measures. We consider MSE value for different values of λ (0.1 to 1) and l (1 to 10).

The corresponding curves for parameter selection are provided in supplementary material (Figs. 1 and 2). Under low photon count, a small variance (σ^2) is considered [14]. The (hyper) parameters used for the state-of-the-art techniques for comparison are considered same as that are reported in the corresponding papers. The Purlet method uses $M = 3$ Wiener filters. The SPIRALTAP method sets regularization parameters and iteration limit as $\tau = 1e-6$ and 100. The TVMAP method uses two parameters which are set empirically as $\lambda = 30$ and $\sigma = 10$. The NLPCA algorithm uses number of cluster $k = 14$ and dimension of the vectorized patch as $N = 20$.

3.3 Quantitative analysis

The SNR comparison results from Fig. 3a shows that the proposed method provides better SNR improvement than other comparative algorithms discussed. Figure 3b shows simulation results of the proposed scheme as compared to five different state-of-the-art methods in terms of correlation coefficient. Figure 3c clearly illustrate that the proposed technique achieves better MSSIM improvement.

The average value of PSNR and MSSIM obtained on different datasets are reported in Table 1. The results of proposed method are highlighted with bold text in Tables 1 and 2 which are better than competitive methods considered. The detailed results are available in supplementary material with different noise levels (α). The runtime performance evaluation of different comparative methods along with proposed one for Fluocell image is shown in Table 2. The proposed IEMD has the computational complexity of $O\left(N \log_2 N\right)$ [21]. The computational complexity of denoising algorithm MPGURE is $O(N)$ [14]. Hence, the overall computational complexity of the proposed algorithm is $O(N) + O\left(N \log_2 N\right)$. Here, N denotes the size of the input.

3.4 Visual analysis of results

The results of proposed scheme along with five different state-of-the-art methods are shown in Fig. 4. For better visualization, the original and corresponding noisy blurred images with microscopic subdetails are shown in Fig. 4a and b. The denoising results obtained using SPIRAL-TAP technique are given in Fig. 4c. It removes the noise by small extent but results in poor contrast of the images. The three circular dots present in the original images are removed by SPIRAL-TAP. The results obtained with SPIRAL-TAP show that central portion of Fluocell image is more affected by noise.

The denoising results of PNLW method are shown in Fig. 4d. The PNLW algorithm improves the visual quality of the considered images. The PNLW method maintains the sub-microscopic details present within the images, but the resulting images are affected by noise. The NLPCA algorithm has retained the structural details as compared with SPIRAL-TAP method but results in low contrast image as shown in Fig. 4e. The results obtained with TV-MAP algorithm is slightly better than NLPCA. The TV-MAP technique shows substantial improvements in noise reduction which can be seen in Fig. 4f.

The PURE-LET method has totally removed the border of Fluo-N3DH-CHO image as shown in first column of Fig. 4g.

Table 1 Average PSNR and MSSIM results of different algorithm

Method	Protein	PSNR	MSSIM	Protein	PSNR	MSSIM	Protein	PSNR	MSSIM
SPIRAL	CERULEAN [Images-153]	17.18	0.3156	DAPI [Images-140]	21.81	0.3897	dSRED [Images-122]	12.47	0.5132
PNLW		22.9	0.3761		22.68	0.4623		15.83	0.6348
NLPCA		19.53	0.3488		24.68	0.4265		13.01	0.5962
TV-MAP		21.53	0.3658		25.02	0.4522		15.23	0.6172
PURE-LET		23.96	0.4012		26.02	0.4823		16.44	0.6802
Proposed		**25.99**	**0.4389**		**28.69**	**0.5033**		**18.87**	**0.7133**
SPIRAL	CFP [Images-103]	11.32	0.3957	GFP [Images-190]	12.87	0.3255	VENUS [Images-166]	10.21	0.4623
PNLW		15.87	0.4795		14.59	0.4155		11.84	0.5512
NLPCA		13.2	0.4092		13.29	0.3622		10.95	0.4952
TV-MAP		14.11	0.4455		14.03	0.3945		11.41	0.5211
PURE-LET		16.2	0.4822		15.26	0.4533		12.62	0.5836
Proposed		**18.43**	**0.5165**		**17.53**	**0.4856**		**14.66**	**0.6132**
SPIRAL	CHERRY [Images-36]	22.97	0.2532	RFP [Images-187]	16.9	0.6122	YFP [Images-30]	19.88	0.4012
PNLW		26.47	0.3422		18.11	0.7055		21.36	0.5055
NLPCA		23.5	0.2871		17.14	0.642		20.13	0.4322
TV-MAP		26.02	0.3075		17.84	0.6822		20.62	0.4822
PURE-LET		27.3	0.3569		19.29	0.7402		22.07	0.5512
Proposed		**29.82**	**0.3952**		**21.71**	**0.7703**		**24.45**	**0.5713**
SPIRAL	CITRINE [Images-37]	13.47	0.3359	Cona Alexa [Images-355]	16.97	0.5123	Cypet [Images-83]	8.13	0.3241
PNLW		18.83	0.4456		20.47	0.5123		11.32	0.3645
NLPCA		15.01	0.3722		18.25	0.5755		9.95	0.3422
TV-MAP		17.23	0.4155		19.83	0.5511		10.74	0.3542
PURE-LET		19.44	0.4615		21.3	0.6022		12.14	0.3722
Proposed		**21.29**	**0.4849**		**23.39**	**0.6202**		**14.67**	**0.4053**
SPIRAL	Phalloidin [Images-118]	24.22	0.5741	YPet [Images-30]	15.02	0.3954			
PNLW		28.14	0.6456		16.32	0.4533			
NLPCA		26.74	0.6012		15.47	0.4122			
TV-MAP		27.11	0.6368		15.92	0.4255			
PURE-LET		29.41	0.6701		17.66	0.4833			
Proposed		**31.66**	**0.7041**		**19.44**	**0.5142**			

Table 2 The runtime performance evaluation

	Method	Time (sec)
Fluocell Image [512 × 512] α=4	SPIRAL-TAP	101.62
	PNLW	61.63
	NLPCA	22.54
	TV-MAP	142.34
	PURE-LET	7.50
	Proposed	**5.30**

The two small circular-shaped Fluorescent tags are totally blurred by PURE-LET method. The PURE-LET approach completely removes the fine structural details like three small dots, and edges present in Saccharomyces cerevisiae species. The outside border of cells within PHC-C2DH-U373 image is removed by PURE-LET method. The PURE-LET method fails to preserve the central portion of Fluocell image which can be seen in Fig. 4g. The PURE-LET reduces noise to great extent with diminishing fine structures within the images.

The denoising results are seen in Fig. 4h; substantiate that the proposed approach has restored the image with superiority and maintained the cell structure. The proposed approach has shown the potential to preserve the finer structural details by removing the noise very efficiently. This can be easily visualized in Fig. 4e with two small dots on Fluorescent protein. For Saccharomyces cerevisiae species shown in the third column, the proposed algorithm has preserved small three dots along with microscopic sub-details. The results obtained for Subcellular microtube substantiate that the proposed algorithm preserves the tiny thread-like structural elements at the same time, it removes the effect of

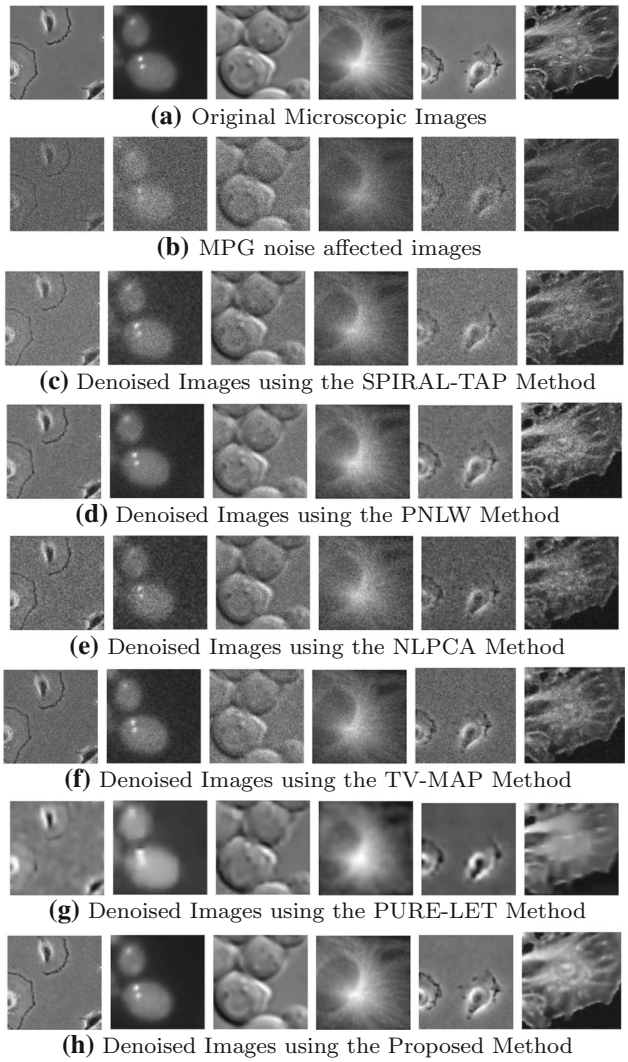

Fig. 4 Visual quality of the fluorescence microscopy images

mixed noise to a great extent. The denoising results obtained for Fluocell clarify that the proposed algorithm reduces the effect of noise to a great extent compared to all considered methods. It also preserves the sub-microscopic details of high biological significance.

4 Conclusions and future works

The proposed technique solves two important problems. Initially, a variance stabilization transformation and multiscale Wiener filtering technique reduces noise and the effect of blurring caused by the point spread function (PSF) of the microscope. In the later stage, IMF adaptive thresholding technique and Cosine similarity index-based IMFs selection scheme reduces the effect of MPG noise, effectively. Further, MPGURE-based optimization also provides a better noise-free estimate of an image by reducing MSD. The proposed algorithm provides better results than existing state-of-the-art methods. Here, the proposed framework can be extended for 3D deconvolution process. The extension to the multiscale Wiener filtering approach and PSF of the microscope can be done for future work. The performance of the proposed scheme is well represented by parameter variations are given in supplementary material (Figs. 1 and 2). Although the change in performance does not vary in large for change in parameter values. However, with noisy conditions, one can use the Monte Carlo Simulation model for parameter estimation. This is the future direction of our work.

References

1. Michalet, X., Pinaud, F., Bentolila, L., Tsay, J., Doose, S., Li, J., Sundaresan, G., Wu, A., Gambhir, S., Weiss, S.: Quantum dots for live cells, in vivo imaging, and diagnostics. Science **307**, 538–544 (2005)
2. Belmont, A.S.: Visualizing chromosome dynamics with GFP. Trends Cell Biol. **11**, 250–257 (2001)
3. Miyawaki, A., Sawano, A., Kogure, T.: Lighting up cells Labelling proteins with fluorophores. Nat. Cell Biol. **5**, 1–7 (2003)
4. Meiniel, W., Olivo-Marin, J.C., Angelini, E.D.: Denoising of microscopy images: a review of the state-of-the-art, and a new sparsity based method. IEEE Trans. Image Process. **27**, 3842–3856 (2018)
5. Rasal, T., Veerakumar, T., Subudhi, B.N., Esakkirajan, S.: Mixed Poisson Gaussian noise reduction in fluorescence microscopy images using modified structure of wavelet transform. IET Image Proc. **15**, 1383–1398 (2021)
6. Louchet C., Moisan L.: Total variation denoising using iterated conditional expectation. In: Proceedings of IEEE Signal Processing, pp. 1592–1596 (2014)
7. Posterior expectation of the total variation model: Louchet, Moisan, L.: Posterior expectation of the total variation model: properties and experiments. SIAM J. Imaging Sci. **6**, 2640–2684 (2013)
8. Sawatzky A., Brune C., Muller J., Burger M.: Total variation processing of images with Poisson statistics. In: Proceedings of Computer Analysis of Images and Patterns, pp. 533–540 (2009)
9. Vonesch, C., Unser, M.: A fast thresholded landweber algorithm for wavelet-regularized multidimensional deconvolution. IEEE Trans. Image Process. **17**, 539–549 (2008)
10. Salmon, J., Harmany, Z., Deledalle, C.-A., Willett, R.: Poisson noise reduction with non-local PCA. J. Math. Imaging Vis. **48**, 279–294 (2014)
11. Ikoma, H., Broxton, M., Kudo, T., Wetzstein, G.: A convex 3D deconvolution algorithm for low photon count Fluorescence imaging. Sci. Rep. **8**, 11489 (2018)
12. Zhang, B., Fadili, J.M., Starck, J.L.: Wavelets, ridgelets, and curvelets for Poisson noise removal. IEEE Trans. Image Process. **17**, 1093–1108 (2008)
13. Kopsinis, Y., McLaughlin, S.: Development of EMD-based denoising methods. IEEE Trans. Signal Process. **57**, 1351–1362 (2009)
14. Le Montagner, Y., Angelini, E.D., Olivo-Marin, J.C.: An unbiased risk estimator for image denoising in the presence of mixed Poisson-Gaussian noise. IEEE Trans. Image Process. **23**, 1255–1268 (2014)
15. Li, J., Luisier, F., Blu, T.: PURE-LET image deconvolution. IEEE Trans. Image Process. **27**, 92–105 (2018)

16. Harmany, Z.T., Marcia, R.F., Willett, R.M.: This is SPIRALTAP: sparse Poisson intensity reconstruction algorithms theory and practice. IEEE Trans. Image Process. **21**, 1084–1096 (2011)
17. Abergel R., Louchet C., Moisan L., Zeng T.: Total variation restoration of images corrupted by Poisson noise with iterated conditional expectations. In: Proceedings of SSVM in Computer Vision, pp. 178–190 (2015)
18. Bindilatti, A.A., Vieira, M.A., Mascarenhas, N.D.: Poisson Wiener filtering with non-local weighted parameter estimation using stochastic distances. Signal Process. **144**, 68–76 (2018)
19. Riffle, M., Davis, T.N.: The Yeast resource center public image repository: a large database of fluorescence microscopy images. BMC Bioinform. **11**, 263–263 (2010)
20. Maska M., Ulman.: A benchmark for comparison of cell tracking algorithms. Bioinformatics **30**, 1609–1617 (2014)
21. Yung, H.W., Chien, H.Y., Hsu, W.V.Y., Kun, H., Men, T.L.: On the computational complexity of the empirical mode decomposition algorithm. Physica A **400**, 159–167 (2014)